Remote Sensing of Environment 295 (2023) 113643

Contents lists available at ScienceDirect

Remote Sensing of Environment

journal homepage: www.elsevier.com/locate/rse

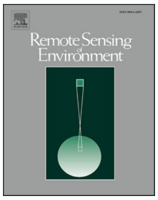

ML based approach for inverting penetration depth of SAR signals over large desert areas

Jun Zhu [a], Guanxin Liu [b,*], Rong Zhao [c], Xiaoli Ding [b], Haiqiang Fu [d]

[a] Department of Surveying Engineering, School of Traffic and Transportation Engineering, Changsha University of Science & Technology, Changsha, China
[b] Department of Land Surveying and Geo-Informatics, Faculty of Construction and Environment, The Hong Kong Polytechnic University, Hong Kong, China
[c] Department of Surveying Engineering, School of Civil Engineering, Central South University of Forestry and Technology, Changsha, China
[d] Department of Geomatics Science and Technology, School of Geosciences and Info-physics, Central South University, Changsha, China

ARTICLE INFO

Edited by Jing M. Chen

Keywords:
Penetration depth
Desert area
Hematite
Kufra Basin
Random forests model

ABSTRACT

Penetration depth of synthetic aperture radar (SAR) signals over a desert is a key parameter to understand the internal properties of the desert. Existing approaches for obtaining the penetration depth require good quality interferometric SAR (InSAR) data of very short temporal and long spatial baselines. Such data are often difficult to obtain in a highly dynamic desert. We propose a new machine learning (ML) based approach for inverting penetration depth of SAR signals over large desert areas by jointly using InSAR, polarimetric SAR (PolSAR) and optical remote sensing data. First, SAR scattering parameters and terrain properties are determined based on PolSAR and Landsat 5 TM multispectral data and a DEM. The penetration depth of SAR signals over a small desert area is obtained based on methods such as using a scattering model. A random forest model is then used to establish the relationship between the SAR scattering parameters and site features, and the penetration depth, and then is used to derive the penetration depth over a large desert area. The approach is applied to calculate the penetration depth of ALOS-1 PALSAR L-band signals for a large part of the Kufra Basin, an area of about 60, 000 km^2. The penetration depths of four types of typical landforms in area (i.e., sandy plains, paleochannels, rocks and man-made features) are discussed in relation to the geological and climatic conditions. The average signal penetration depths over the paleochannels, sandy plains, and rocks and man-made features are 2.84 m, 1.97 m, 1.21 m, respectively. It is found that the backscattering coefficient, dielectric constant, surface roughness and mineral composition are the most important parameters in determining the signal penetration depths. An interesting point is that the existence of hematite in the sand can increase the dielectric dissipation of the sand medium and shorten the signal penetration depth.

1. Introduction

Deserts take up about one third of Earth's land surface (United States Geological Survey (USGS), 2022). It is important to study the deserts to understand their characteristics and how they change over time. In addition to using optical remote sensing data to study the various surface parameters of the deserts, such as aeolian activities and dune migration (Ali et al., 2020, 2021, 2022), Synthetic aperture radar (SAR) data have been used to investigate the internal properties of deserts (e.g., dielectric properties, soil roughness, particle size) (Mccauley et al., 1982; Schaber et al., 1997; Lüning et al., 1999; Robinson et al., 2006; Paillou et al., 2009). When SAR data are used to study deserts, it is essential to know the signal penetration depth (SPD). In early 1980s, NASA/JPL launched the first Shuttle Imaging Radar missions (SIR-A and SIR—B). It was demonstrated that the L-band (1.3 GHz) SAR signal could retrieve subsurface information of the Sahara Desert to a depth of a few centimeters to two meters (Mccauley et al., 1982; Schaber et al., 1986). Schaber et al. (1997) delineated the subsurface structure of sand sheet in Bir Safsaf using multi-frequency polarimetric SIR-C/X SAR images. It was shown that the imaging depth was 0.1–0.3 m for the X-band (10 GHz), 0.2–0.5 m for the C-band (5.3 GHz) and 0.8–2.0 m for the L-band (1.3 GHz) signals. The SPDs in arid sediments have also been investigated in the Yuma desert of Arizona (Schaber, 1999), Nevada desert (Farr et al., 1986), Badain-Jaran desert (Guo et al., 1986, 2000), Selima sand sheet (Elachi et al., 1984), and Western Desert of Egypt (Gaber et al., 2011). These studies determined the penetration depths of signals

---

* Corresponding author.
E-mail address: 22040393r@connect.polyu.hk (G. Liu).

https://doi.org/10.1016/j.rse.2023.113643
Received 16 December 2022; Received in revised form 5 May 2023; Accepted 21 May 2023

of different frequencies by carrying out field work such as burying corner reflectors under the deserts and therefore were laborious and time-consuming.

Studies in hyper-arid areas also took advantage of SAR intensity images (e.g., El-Baz et al., 2000; Ghoneim and El-Baz, 2007; Sternberg and Paillou, 2015), elevation derived from interferometric SAR (InSAR) data (e.g., Dall, 2007; Elsherbini and Sarabandi, 2010; Wang et al., 2014, 2015; Xiong et al., 2017) and parameters derived from polarimetric interferometric SAR (PolInSAR) data (e.g., Dan, 1998; Gaber et al., 2017; Natale et al., 2019). Good quality PolInSAR data over desert areas are however difficult to obtain. Consequently, such data have not been used much for determining the SPD over desert areas. InSAR, including differential InSAR and scattering models are used more often for this purpose. Although phase errors due to, e.g., atmospheric delays and orbital errors are considered in InSAR-based methods, residual phase errors can still mix up with the phase of penetration depth, affecting the estimation accuracy (Xiong et al., 2017). The scattering model approaches are usually based on signal refraction at the interface between the sand and the air and the scattering loss in the sand medium. Considering the change in the signal propagation velocity in the medium, Wang et al. (2015) proposed a modified two-layer model for InSAR height measurement in sand-covered areas. The model however needs to fix various parameters that sometimes are not easy to determine accurately. Liu et al. (2020) presented an infinite volume model (IVM) that established the relationship between the InSAR coherence and the SPD for loose sand media. A framework was proposed based on the assumption of a homogeneous infinitely deep volume and considering the InSAR illumination geometry to invert the penetration depth of L-band signal (1.27 GHz).

The IVM will be employed in this paper to obtain the sample SPD in a small desert area although other approaches such as using buried corner reflectors can also be used. Both differential InSAR and model (e.g., IVM) based approaches require InSAR data to be acquired over a short time interval to reduce the coherence loss caused by the highly dynamic surface of a desert, and a long spatial baseline to achieve a small ambiguity height. Unfortunately, such data are difficult to obtain in a large desert area with the current SAR systems. To enable large-area penetration depth inversion in a desert, multi-source remote sensing data will be used. It is well known that microwave SAR signals in different polarization modes are sensitive to the shapes, distribution and dielectric properties of scatters while optical images are advantageous in revealing the texture and spectrum information of the surface. If the SPDs can be retrieved over a small sample area, and the relationship between the penetration depth and the scattering parameters can be established, inversion of penetration depth over a large desert area based on machine learning (ML) model will be possible.

In this paper, we first select reasonable parameters from multi-source data including polarimetric SAR (PolSAR) data, optical data and external DEM. The sample SPD is obtained from the IVM and is validated in an indirect way. Subsequently, the relationship between the training parameters and the penetration depth over a sample desert is established based on the random forests (RF) model. At last, the SPD over a large desert area can be further predicted through the trained model. Due to a lack of in situ measurements and other already published data to verify the absolute accuracy of the SPD results, we validate the reliability of our experimental methods and results by using scatterplots to further show the relationship and patterns between SPDs and training parameters. The predicted penetration results in different land cover are also discussed in detail. The aim of this research is to propose a new strategy that can retrieve the penetration depth in a large desert area, which can effectively overcome the shortage of InSAR data in deserts and provide a new way for investigating the geometric structure and physical properties of the sandy medium.

Following this introduction, the rest of this paper will be organized as follows. Section 2 will describe the study area and the experimental data. Section 3 will introduce the proposed inversion strategy, including signal scattering process in a sand medium and extraction of the critical parameters. Sections 4 and 5 will present the results and some discussions while conclusions will be given in Sections 6.

2. Study area and dataset

2.1. Study area

The study area (22°N - 25°N, 22.5°E - 25.5°E) is about 60, 000 km^2, located in the low-lying Kufra Basin in the southeast of Libya, with its eastern part connected to Jabal Oweinat Mountain and Gilf Kebir Mountain, and its southern part blocked by Tibesti Mountains (Fig. 1(a)). The surface is mainly monotonously flat sandy plains (Fig. 1(b)). The rainfall in the area is less than 1 mm/yr and plants are almost nonexistent except in some oases. The loose sand is eroded and redistributed into a series of complex aeolian sediments by the strong winds from NE direction (Davis et al., 1993). The plains show mottled intermediate responses on the SAR amplitude images (Fig. 1(c)). The Nubian Sandstone Series beneath the sandy plains are the principal source for most of the Pleistocene sand and gravel deposits (Davis et al., 1993), composed primarily of sandstones, sand and clay (Hermina, 1990; Lüning et al., 1999). There are huge rock outcrops, or broken terrains formed by shallow sand and complicated gullies (Fig. 1(b1) and (b2)), which show a very bright response on the SAR amplitude images (Fig. 1(c)). In Fig. 1 (b3), a long palaeodrainage system buried in the sand layer, which is invisible on the Google Earth image, shows an extremely dark response on the SAR amplitude images (Xiong et al., 2017). Besides the main channel, some branches are also visible in the L-band images. The continuous palaeodrainage system with a length of about 900 km, called Kufra river, has been accurately delineated (Paillou et al., 2003, 2009) in the Kufra Basin and a huge aquifer system below that has been found by geophysical exploration (Robinson et al., 2006, 2007). This paleodrainage system is inconsistent with that recorded in the HYDRO1K database of the United States Geological Survey (USGS), indicating that it may be of subsurface origin (Robinson et al., 2006). The Jauf City, located in northwest of the study area, is the capital of Kufra Province. It lies in the largest oasis in the Kufra Basin, including different landforms like buildings, farmlands and grasslands (Fig. 1(b4)). The area shows very bright responses, similar to the rock outcrops.

2.2. Dataset

2.2.1. ALOS-1 PALSAR data

ALOS-1 (Advanced Land Observing Satellite – 1) was an Earth observation satellite launched and operated by Japan Aerospace Exploration Agency (JAXA). The satellite carried three remote sensing instruments, the along-track Panchromatic Remote-sensing Instrument for Stereo Mapping (PRISM), the Advanced Visible and Near-Infrared Radiometer type 2 (AVNIR-2), and the polarimetric Phased Array L-band Synthetic Aperture Radar (PALSAR). The main specifications of the ALOS-1 PALSAR images used in this research are shown in Tables 1 and 2, respectively. To obtain the penetration depth based on the IVM in the area indicated by the blue rectangle in Fig. 1(b), two SAR images are used to form an interferometric pair. The SAR data used are the same as that deployed in Liu et al. (2020). The 12 SAR images for the areas indicated by the three red rectangles in Fig. 1(b) are from different satellite paths and frames. All the SAR data are in the Fine Beam Dual (FBD) polarization modes, i.e., horizontal-horizontal (HH) and horizontal-vertical (HV). The HH-polarized data is deployed to retrieve the SPDs due to its stronger penetration ability and higher coherence. The incidence angles were almost fixed and the resolutions of the images after multilook operation (range:azimuth = 2:10) are about azimuth × range = 30 m × 30 m.

2.2.2. Landsat 5 TM data

Landsat 5 was a NASA's multispectral imaging mission that carried

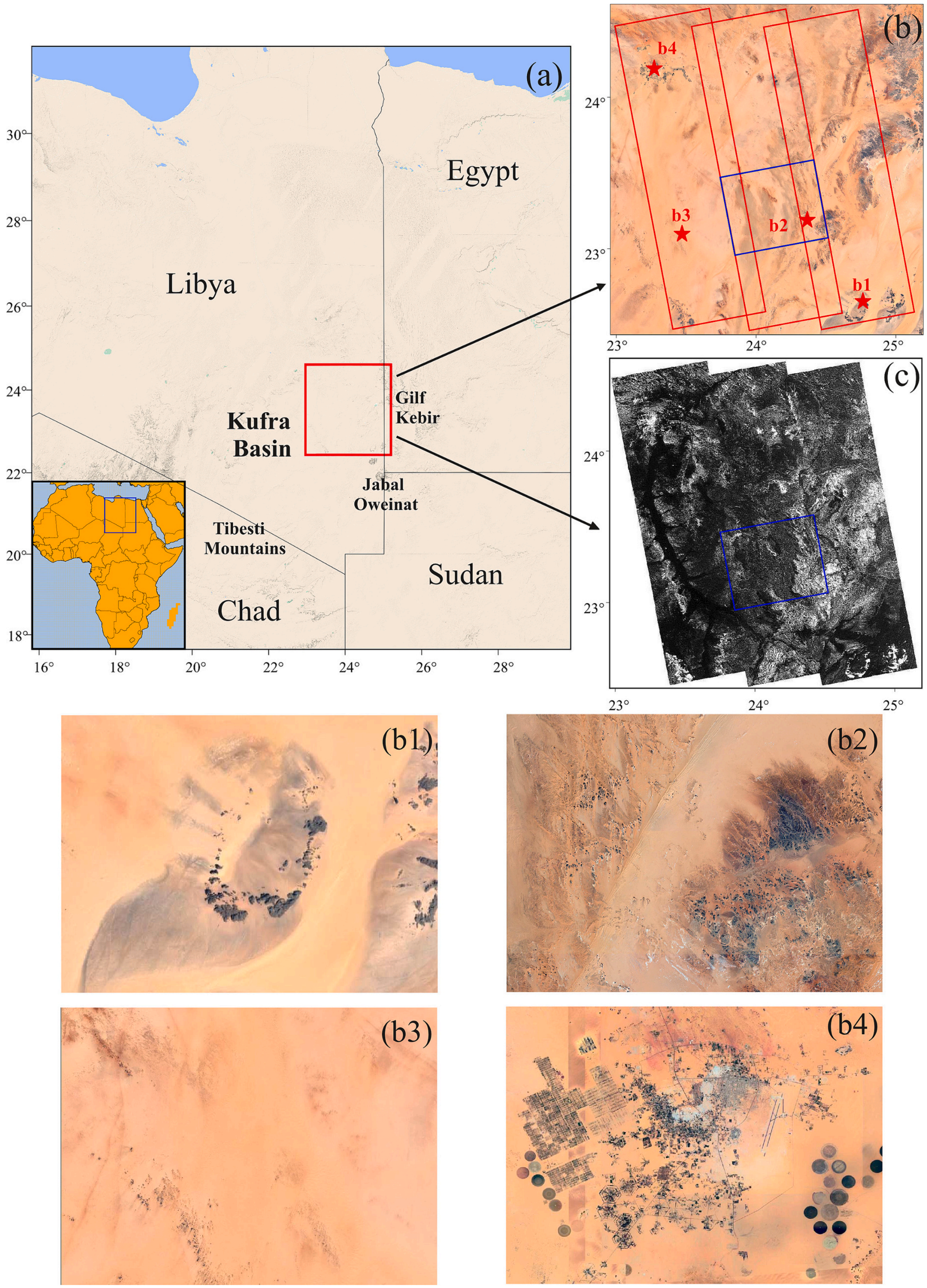

Fig. 1. (a) Location of the study area; (b) ALOS-1 PALSAR (Phased Array L-band Synthetic Aperture Radar) SAR image coverages (red rectangles) over the study area. The base map is the Google Earth image. The blue rectangle represents the sample desert area where the penetration depth is determined with a scattering model; (c) amplitude of HH-polarized ALOS-1 PALSAR images; (b1) (b2) (b3) (b4) are the four selected areas marked by the pentagrams in (b), corresponding to rock outcrops, broken topography, buried drainage channels and man-made features, respectively. (For interpretation of the references to color in this figure legend, the reader is referred to the web version of this article.)

Table 1
ALOS-1 PALSAR data used for inverting the sample desert area (blue rectangle in Fig. 1(b)).

Acquisition date	Orbit number	Path	Frame	Polarization	Spatial baseline (m)	Temporal baseline (d)
2008.07.29	13,811	626	450	HH&HV	1110	46
2008.09.13	14,059					

Table 2
ALOS-1 PALSAR data used for the large study area (three red rectangles in Fig. 1(b)).

Acquisition date	Orbit number	Path	Frame	Polarization	Incidence angle (°)	Initial azimuth/range resolution (m)
2008.07.29	13,811	625	440	HH&HV		3.16/9.37
2008.08.27	13,388	626	–		38.72	
2008.09.30	14,307	627	470			

the Thematic Mapper (TM) imaging sensor. The sensor provided images in seven reflectance bands with a spatial resolution of up to about 30 m. Nine Landsat 5 TM images (Table 3) that covered the study area and had close acquisition time to those of the SAR images are used in this study. The optical images are cropped to the size of the SAR images and the resolution after resampling is the same as the SAR images.

The reflectance of the different bands is first calculated after radiometric and atmospheric corrections. The data are then used for classifying the ground objects and for determining the mineral composite of the study area. Bands 3, 2, and 1 are used to form natural images for better interpretation of the surface features, while the combination of bands 7, 4, and 1 is used to discriminate the mineral composite.

2.2.3. *DEM data*

The AW3D 30 DEM was developed by JAXA based on data from the PRISM sensor also onboard the ALOS-1. Therefore, the data acquisition time of PRISM was consistent with that of the SAR images acquired by PALSAR. The resolution of the DEM is approximately 30 m.

3. Methodology

The critical step of the method is to extract the parameters of the desert that can characterize the penetrability of the SAR signals. We will first examine the scattering process of SAR signals in a sand medium to illustrate the relationship between the SPDs and the scattering parameters of the sand layer. After that, the characteristics of the ground will be studied based on PolSAR and optical remote sensing data, and the SPDs in the sample desert area will be determined based on the IVM. A random forests model will subsequently be deployed to establish the relationship between the ground characteristics and the penetration depth. The SPD of the whole Kufra Basin will finally be computed based on the RF model. The proposed method is depicted in the flowchart in Fig. 2.

Table 3
Key parameters of Landsat 5 TM data.

Acquisition date	Number of images	Bands	Spectral ranges (μm)	Spatial resolution (m)	Product type
2008.08.17	3	band1 (Blue)	0.42–0.52	30	Level 1.0
		band2 (Green)	0.52–0.60		
2008.08.24	3	band3 (Red)	0.63–0.69		
		band4 (Near IR)	0.76–0.90		
2008.08.26	3	band5 (SW IR)	1.55–1.75		
		band6 (LW IR)	10.40–12.50		
		band7 (SW IR)	2.08–2.35		

3.1. *Signal scattering in desert*

A desert layer is usually composed of compacted sand. The SAR signal is refracted at the air-sand interface and the propagation velocity in the sand changes significantly due to the very different dielectric properties in the sand and in the air. The refractivity in the sand is determined by the dielectric constant of the sand layer, and the scattering or attenuation of the signal is related to the particle size, density and moisture content of the sand. The signal penetrability mainly depends on two factors, i.e., the attribute of the sand layer and the parameters of the SAR system. The propagation process can be divided into four parts, backscattering at the air-sand interface σ_{as}, volume scattering in the sand mediumσ_v, interaction between a bedrock and sandσ_{gv}, and backscattering by the bedrock $\sigma_g^{'}$ in the case that the SAR signal penetrates through the sand layer,

$$\sigma = \sigma_g^{'} + \sigma_{gv} + \sigma_v + \sigma_{as} \tag{1}$$

In most cases, the SAR signal cannot penetrate through the desert layer, therefore only two of the components (σ_{as} and $\sigma_g^{'}$) need to be considered. As for the SAR system, the smaller the incidence angle is and the lower the frequency is, the stronger the penetration will be. For a given SAR system, these parameters remain almost unchanged. Therefore, the penetrability of a SAR signal is mainly determined by the physical properties of the desert layer.

3.2. *Sample penetration depth based on InSAR*

The SPDs in a sample area are required to be used as the training data to develop the RF model. SPD models have been developed based on coherence or interferometric phase for ice-covered (Sharma et al., 2013; Banda et al., 2016) and forest areas (Schlund et al., 2019). An IVM that builds a relationship between the coherence and SPD has also been developed (Liu et al., 2020) and will be used in this study to derive the SPDs of the sample area. When the SAR signal propagates in a lossy medium (Fig. 3), the SPD is a function of the vertical distribution of the volume (Ulaby et al., 1981),

$$d_{pen} = \frac{cos\theta_r}{2\mu} \tag{2}$$

where d_{pen} is the two-way penetration depth; θ_r is the refraction angle and $cos\theta_r$ represents the deviation from the vertical propagation distance after the refraction at the air-sand interface; μ is the power extinction coefficient.

The interferometric vertical effective wavenumber k_z links the interferometric phase φ and the range to the scatterer (Sharma et al., 2013),

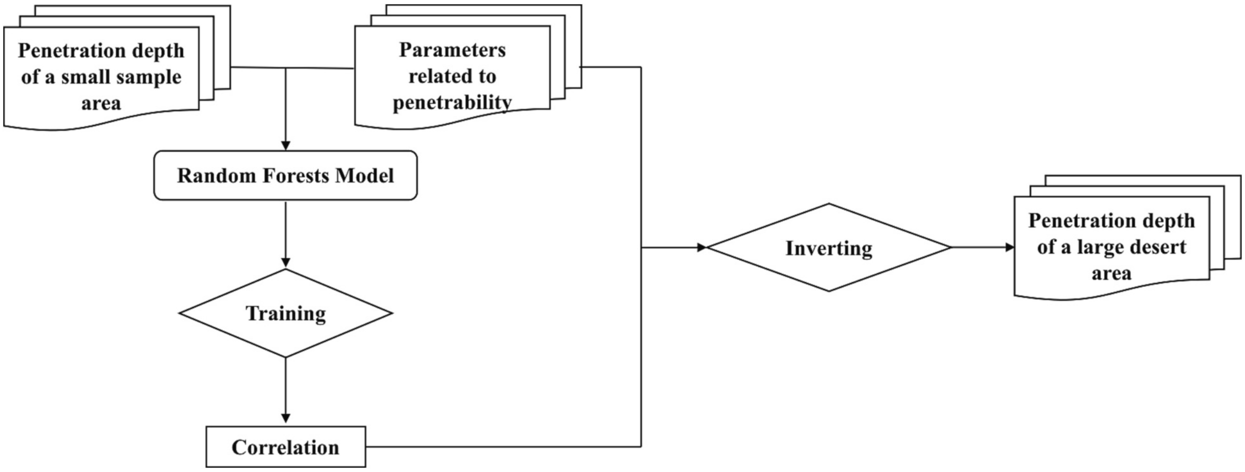

Fig. 2. Overall flowchart of the proposed method.

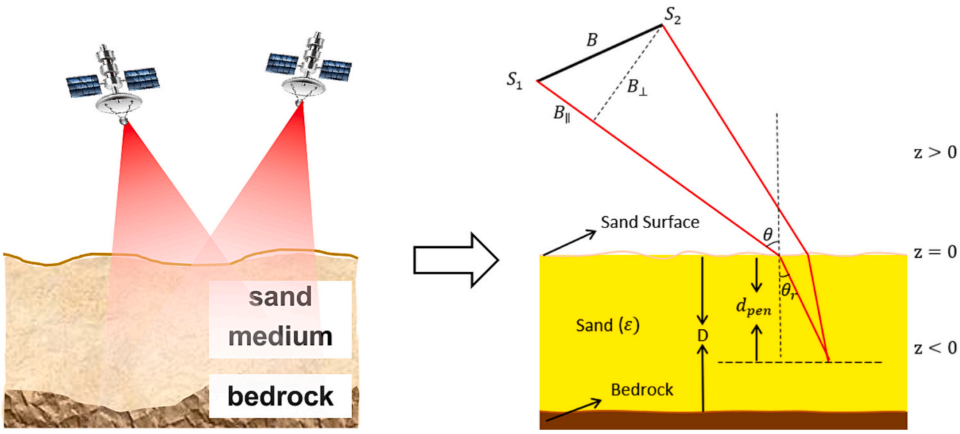

Fig. 3. InSAR illumination geometry based on the two-layer model. The desert surface is defined as the reference datum, i.e., $z = 0$, and the extents of the sand and air are defined by $z < 0$ and $z > 0$, respectively. D is the thickness of the desert layer and ε represents the dielectric constant.

$$k_z = \frac{\partial \varphi}{\partial z} = \frac{4\pi}{\lambda}\frac{B_\perp}{Rsin\theta} \tag{3}$$

where λ is the radar wavelength; R is the slant range and $B_\perp$ is the perpendicular baseline. For a lossy sand medium, k_z should account for both the propagation and refraction of the SAR signal and can be expanded into the following (Dall, 2007),

$$k_{zvol} = k_z \frac{\varepsilon cos\theta}{\sqrt{\varepsilon - sin^2\theta}} \tag{4}$$

Combining Eqs. (3) and (4), the volumetric correlation coefficient γ can be directly related to the SPD d_{pen} (Liu et al., 2020),

$$\gamma = \frac{1}{2} + \frac{1}{2}\frac{1 - jk_{zvol}d_{pen}}{1 + jk_{zvol}d_{pen}} \tag{5}$$

Where j is the imaginary unit. Normalizing the coherence by the interferometric phase at the volume surface, the coherence becomes zero when the SPD equals $1/k_{zvol}$ and up to 1 when there is no penetration, making it possible to derive the SPD from the coherence phase,

$$d_{pen} = \frac{\sqrt{|\gamma|^{-2} - 1}}{|k_{zvol}|} \tag{6}$$

3.3. Extraction of scattering parameters

We used 12 ALOS PALSAR images to extract the key scattering parameters of the study area including the backscattering coefficient, dielectric constant and surface roughness. The elevations of the desert surface are extracted from ALOS World 3D – 30 m (AW3D 30) DEM. The reflectivity of selected bands is extracted based on multispectral Landsat 5 Thematic Mapper (TM) images.

3.3.1. Extraction of scattering parameters from PolSAR data

The following scattering parameters are extracted from the PolSAR data,

Backscattering coefficient. The backscattering power to radar signals is mainly determined by the properties of the sand layer including the particle size, density and humidity. The phenomena of scattering, absorption and attenuation can be reflected in the amplitude images when the SAR signals interact with the volume. The amplitude is highly sensitive to the attributes of a sand medium, resulting in more obvious change in the pixel brightness than that of an optical image (Schaber, 1999). In general, the backscattering coefficient has a small magnitude and can vary significantly. Therefore, to make the values distribute more uniform and reduce the outliers, the backscattering coefficient is usually expressed in the form of dB,

$$\sigma^{\circ}_{dB} = 10log_{10}\sigma \tag{7}$$

Dielectric constant and surface roughness. The dielectric constant is closely related to the attenuation of the signal power in the medium, and it reflects the properties of scattering, absorption and transmission of the electromagnetic wave. In general, a larger dielectric permittivity leads to stronger attenuation and weaker penetrability. The dielectric constant is composed of a real part and an imaginary part. The former is related to the scattering and attenuation of the electromagnetic wave and is mainly determined by the moisture content, while the imaginary part is controlled by the soil salinity and is almost always less than 0.05 (Matzler, 1998, Matzler and Murk, 2010; Hallikainen et al., 1985; Dobson et al., 1985; Hoekstra and Delaney, 1974). For a lossy sand medium, the imaginary part is far smaller than the real part and is therefore ignored in this study.

The surface roughness can characterize the scattering properties of a bare surface (Archer and Wadge, 2001; Paillou et al., 2003; Charlton and White, 2006). In general, surface roughness is described by the root mean square height (*s*) and the correlation length (*l*), which represent the geometric characteristics of a random surface in the vertical and horizontal directions, respectively. *s* measures the surface roughness (relative to the wavelength) of a desert surface (Peake and Oliver, 1971). Different objects such as rock outcrops and sand layer can be easily distinguished with *s*. On the other hand, *l* is often unreliable due to too few available surface profiles or the low sampling resolution of the DEM. Furthermore, it has negligible influence on the scattering of low-frequency SAR signals (e.g., the L-band) in the desert (Charlton and White, 2006). This parameter will therefore not be considered in this study.

To retrieve the dielectric constant and surface roughness, a semi-empirical model proposed by Oh (2004) for bare soil surface is used. The model performs well over a wide range of soil surfaces. The moisture content will be retrieved directly from the model and then it can be converted into the soil dielectric constant based on a typical conversion model (Topp et al., 1980). The cross-polarized backscattering coefficient, without considering the correlation length, is modeled as (Oh, 2004),

$$\overset{\circ}{\sigma}_{hv} = 0.11 m_v^{0.7} (cos\theta)^{2.2} \left[1 - exp\left(-0.32(ks)^{1.8}\right)\right] \tag{8}$$

$$p = \frac{\overset{\circ}{\sigma}_{hh}}{\overset{\circ}{\sigma}_{vv}} = 1 - \left(\frac{\theta}{90}\right)^{0.35 m_v^{-0.65}} \bullet exp\left(-0.4(ks)^{1.4}\right) \tag{9}$$

$$q = \frac{\overset{\circ}{\sigma}_{hv}}{\overset{\circ}{\sigma}_{vv}} = 0.095\left(0.13 + sin(1.5\theta)^{1.4}\right)\left\{1 - exp\left(\left[-1.3(ks)^{0.9}\right]\right)\right\} \tag{10}$$

where $\overset{\circ}{\sigma}_{hv}, \overset{\circ}{\sigma}_{hh}, \overset{\circ}{\sigma}_{vv}$ are the simulated backscattering coefficients; p and q are the co-polarized and cross-polarized ratios, respectively; m_v is the moisture content; k is the wavenumber ($k = 2\pi/\lambda$) and ks is usually used as an integrated soil roughness parameter (in the case of l being absent); and θ is the incidence angle.

The input parameters in such a semi-empirical model include the incidence angle, the moisture content and surface roughness, among them the incidence angle is unchanged and fixed. After that, a 2-D look-up table is generated according to Eq. (8) when the range and the step size of m_v and s are given. In this case, the simulated HH-polarized backscattering coefficient can then be calculated at each specific m_v and s from the HV-polarized backscattering coefficient with the ratio between p and q,

$$\overset{\circ}{\sigma}_{hh} = \overset{\circ}{\sigma}_{hv} \bullet \frac{p}{q} \tag{11}$$

Taking the minimum difference between the simulated backscattering coefficient and that obtained from the SAR images as the criterion, the corresponding m_v and s of each pixel can be retrieved (Oh, 2004),

$$min\left\|\overset{\circ}{\sigma}_{hh} - \sigma_{hh}\right\| \tag{12}$$

After obtaining the moisture content, Topp's calibration model is used to calculate the dielectric constant (Topp et al., 1980),

$$\varepsilon = 3.03 + 9.3 m_v + 146 {m_v}^2 - 76 {m_v}^3 \tag{13}$$

3.3.2. *Extraction of surface features from optical images and DEM*

Parameters such as the mineral composite, type of an object, elevation are extracted from multispectral optical images and a DEM.

Mineral composite: In arid areas, most TM-band false-color images show saturated patterns and therefore some valuable information is lost when applying a standard linear contrast stretch approach. To better describe the subtle change in the mineral composite, such as the existence of carbonate, sulfate and minerals containing Fe^{2+} or Fe^{3+}, based on the color variation of a composite image, a decorrelation-stretch (Gillespie, 1986) is deployed to the TM bands 7, 4, 1 and a false-color composite image is generated by assigning red, green, and blue colors to the three bands, respectively. The change in the mineral component may lead to different power attenuation and penetrability.

Type of objects: Objects in the study area including rock outcrops, sand layers and man-made features are classified based on the reflectivity of the objects in the natural color image composite of bands 3(R), 2 (G) and 1(B).

Elevation: Surface geometric features like elevation are extracted from a mosaic DEM. Although there is no direct relationship between the elevation and the SPD, the elevation information helps distinguish the type of the objects and landforms and, to some extent, knowledge about the height, orientation and slope of a sand dune, especially in Kufra basin.

3.4. *Deriving penetration depth over the large desert area*

Random forests are an effective prediction tool based on statistical learning theory (Breiman, 2001). It has been widely used due to its high-training speed, good prediction accuracy and strong generalization ability. We therefore use RF to investigate the relationship between the obtained parameters of the area and the SPDs.

In the sample desert area, the reflectivities of spectral bands 1, 2, 3, 4 and 7 of Landsat TM images are first calculated after preprocessing options like radiometric calibration and atmospheric correction and are geo-registered with the SAR images to the WGS84 geographic coordinate system. It's noteworthy that bands 5 and 6 are not used in our study because their reflectivities hardly change in our study site and don't contribute to the improvement of training accuracy. Meanwhile, ALOS-1 PALSAR images with different polarizations are used to extract the backscattering coefficients after co-registration and multi-look processing. Due to the strong penetrability and the high echo power of the co-polarized (HH) signal and conversely the severe dissipation of the cross-polarized (HV) signal inside the sand medium, the backscattering coefficient ratio between the two polarization modes is used to improve the training accuracy. The backscattering coefficients are also employed to derive the dielectric constant and surface roughness by using the Oh. inversion model. The elevation of AW3D DEM is used as an auxiliary parameter. Therefore, a total of nine training parameters are derived. On the other hand, the penetration depth of the sample desert area is derived from the infinitely deep volume model. The RF is applied to build the relationship between the training parameters and the sample penetration depth.

Once the relationship is effectively established, we can use the trained model to predict the penetration depth in our study area. The study area is covered by 12 SAR images in three paths (i.e., path 625, 626 and 627), and each path includes four SAR images, as shown in Fig. 1(b) and Table 2. The four SAR images in the same path are firstly mosaic along the azimuth direction and in the later processing, we process the SAR images path by path. The method of acquiring the training parameters in each path is the same as that used in the sample desert area. In each path, we applied the trained model to predict the penetration depth. Subsequently, the penetration depth results in three paths can be derived. We then mosaic the results of three paths, among which the penetration depth at the overlapping area is obtained by averaging the values of two adjacent paths. Finally, the penetration depth map of ALOS-1 PALSAR L-band signals in the Kufra basin can be generated. The detailed workflow is given in Fig. 4.

4. Results

4.1. Validation of the sample penetration depth

In Kufra basin, there is no in situ penetration depth and other already published data sets, therefore we aim to validate the derived sample penetration depth in an indirect way. The elevation of the reconstructed ALOS-1 PALSAR DEM plus the sample SPD are regarded as the desert surface elevation (hereafter called synthetic surface elevation) and the synthetic results are used to compare with the reference elevation provided by the Geoscience Laser Altimeter System (GLAS)/ Ice, Cloud, and land Elevation Satellite L2 Global Land Surface Altimetry Data Version 34 (GLAH 14) (Satgé et al., 2015). A total of 227 ICESat/GLAS points with a 70 m diameter over the sample area are obtained. The laser points are acquired on 18 October 2008 and their geolocation is shown in Fig. S1 of the Supplementary Materials. We evaluate the absolute vertical accuracy of the PALSAR DEM and the synthetic surface elevation to validate the reliability of the derived sample SPD.

In order to construct the PALSAR DEM, we need to remove other phase errors first. The 30 m resolution SRTM is used to simulate the topography phase and the quadratic polynomial is applied to remove the orbit error phase. The interferogram (Fig. S2(a)) doesn't show noticeable artifacts along the azimuth direction. Therefore, the ionospheric effects can be ignored. The troposphere delay is primarily caused by Precipitable Water Vapor (PWV). In hyper-arid regions, the spatiotemporal variation of the PWV is likely to be smaller than that in other areas due to the lower humidity. To confirm this, the zenith delay maps provided by Generic Atmospheric Correction Online Service (GACOS) (Yu et al., 2018) are used to calculate the troposphere delay (Fig. S2(c)). We can see that the spatial variations of troposphere delay are much smaller than 0.1 rad (about 0.03 rad), which corresponds to an elevation variation of 0.25 m when the perpendicular baseline is 1110 m. Consequently, considering that new systematic errors may be imported if the troposphere delay (GACOS provided) is not accurate enough, we do not subtract the troposphere delay from the interferogram. After that, the remaining phase components can be converted to height information and a PALSAR DEM can be then reconstructed.

The accuracy of the PALSAR DEM and the synthetic surface elevation is quantitatively analyzed by comparing with the ICESat/GLAH14 elevation, as shown in Fig. 5. At the points at both ends of the ICESat transect, corresponding to rock areas, the elevation of PALSAR DEM is approximate as that of ICESat points. While in the middle part of the transect, corresponding to the sandy plains and channels, the DEM height is much smaller than the ICESat elevation. However, after adding the derived sample SPD to the DEM, the synthetic surface elevation shows a consistent pattern with the ICESat elevation and also their elevation difference becomes smaller. Further, we calculate the root-mean-square error before and after adding the penetration depth to the PALSAR DEM, and the RMSE has decreased from 7.82 m to 3.34 m, which shows that the SPD derived by the IVM is reliable and convinced.

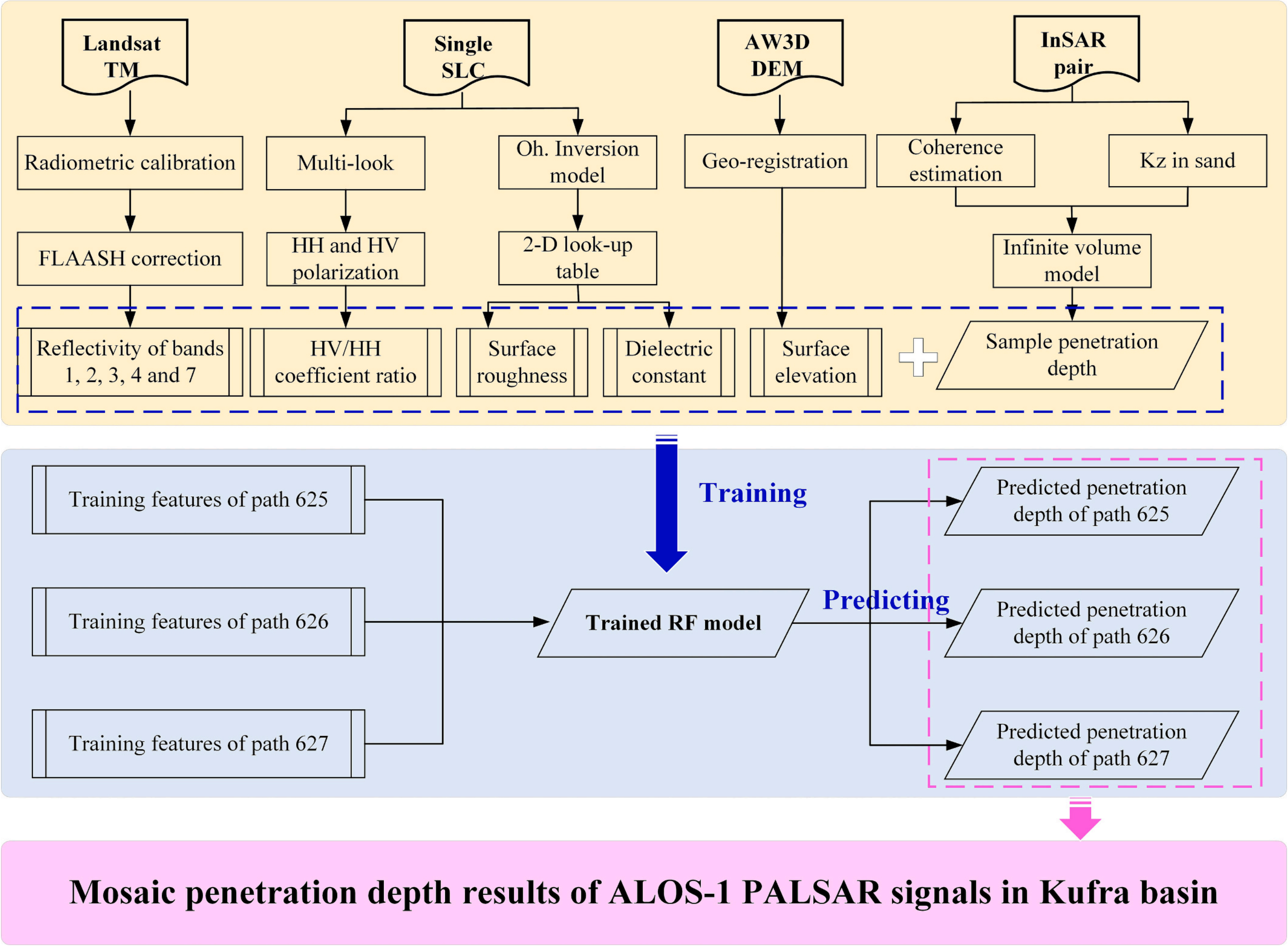

Fig. 4. Workflow for penetration depth inversion.

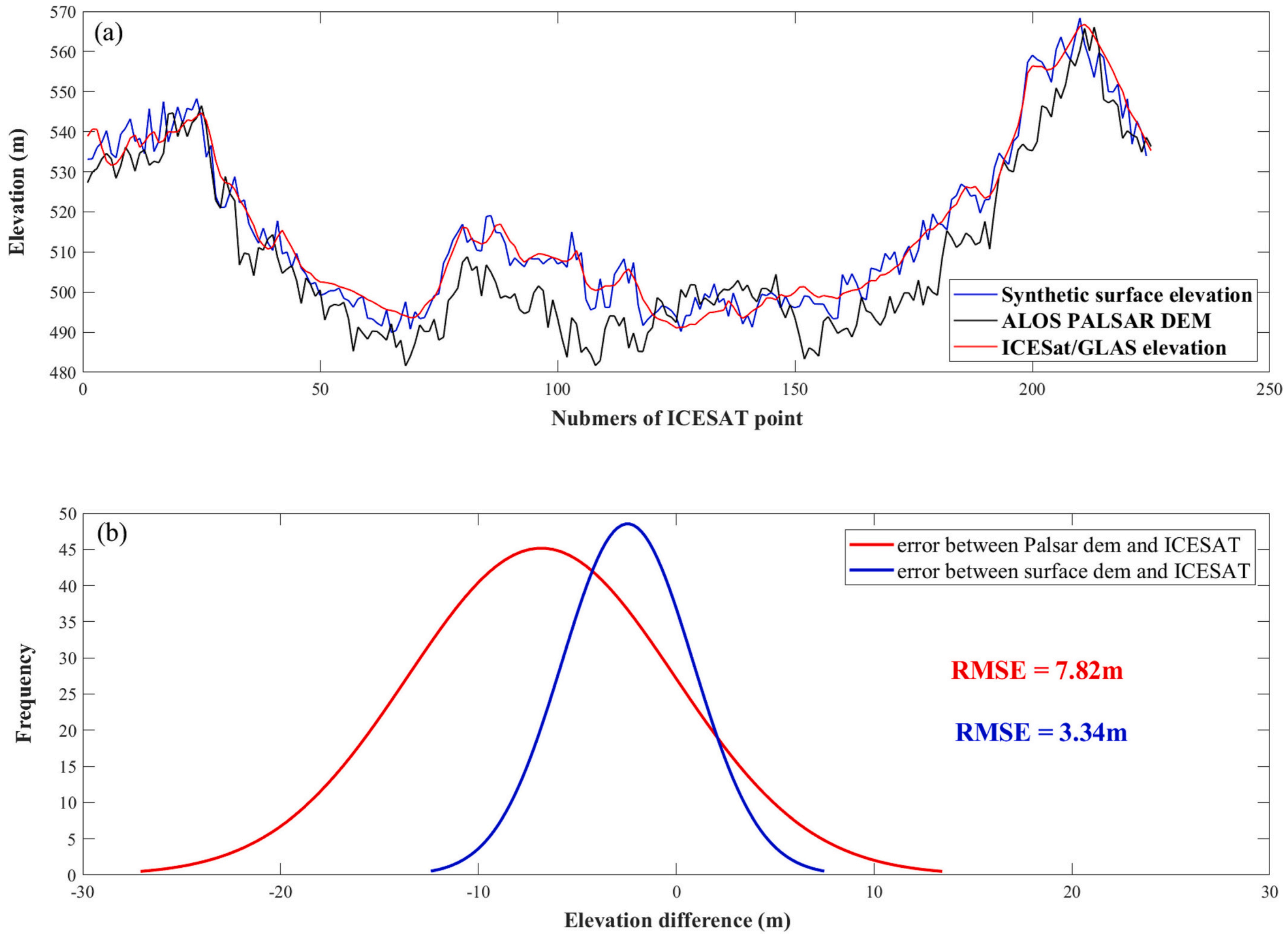

Fig. 5. (a) The comparison between the PALSAR DEM, the synthetic surface elevation and the ICESat/GLAS elevation along the ICESat transect; (b) Statistical analysis of the comparison.

4.2. Training results

The moisture content in the small sample desert area, about 5, 000 km^2, is calculated based on the semi-empirical model discussed earlier. When building the 2-D look-up table, the initial and end value of m_v is set to 0.001 cm^3/cm^3 and 0.15 cm^3/cm^3 with a step size of 0.001, and the value of ks is set to 0.05 and 5 with a step size of 0.01, respectively. After the moisture content is retrieved, it is then converted into the dielectric constant to correct the vertical effective wavenumber in sand medium (Fig. 6(b)). The sample SPDs (Fig. 6(c)) were derived with Eq. (6) based on the coherence of the HH-polarized interferogram (Fig. 6(a)). The coherence map apparently shows different coherence related to the different features in the desert (Liu et al., 2020).

The backscatter coefficient ratio between HV- and HH-polarized signals (i.e., σ_{HV}/σ_{HH}) is used to improve the training accuracy (Fig. 7(a)). The derived dielectric constant and surface roughness determined based on the semi-empirical inversion model are given in Fig. 7(b) and (c), respectively. The distributions of σ_{HV}/σ_{HH}, ks and ε are correlated as they have similar responses to the SAR signals. Fig. 7(d) gives the

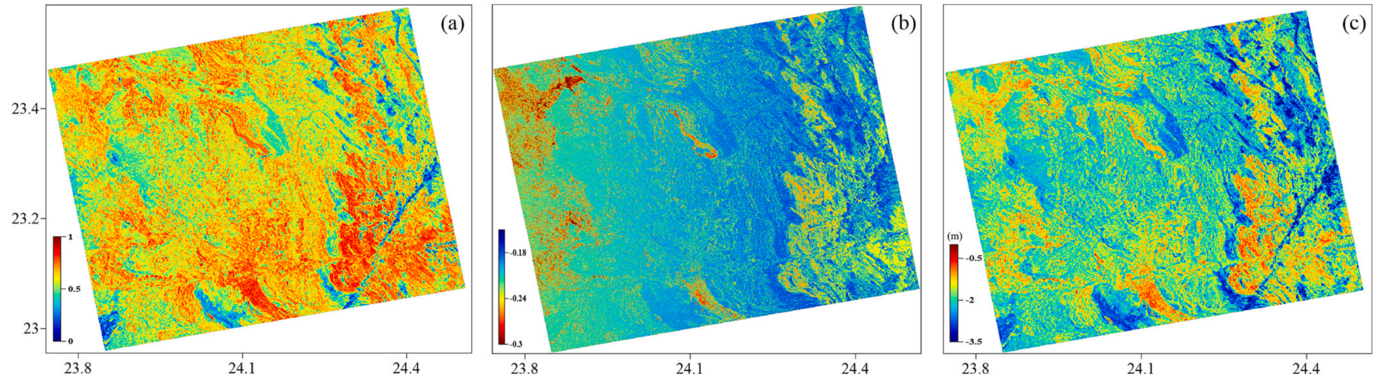

Fig. 6. (a) Coherence map, (b) Vertical effective wavenumber in sand medium, and (c) Inverted penetration depth of the sample area.

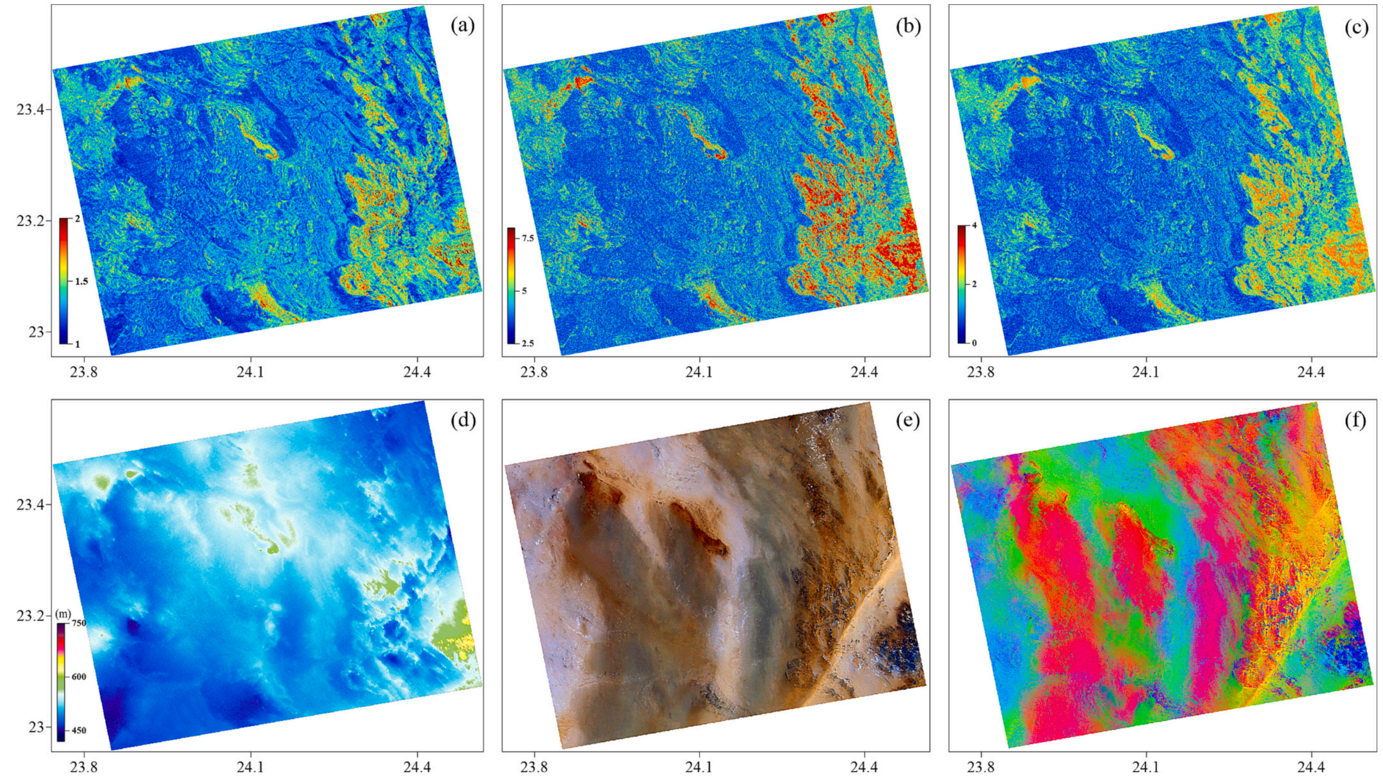

Fig. 7. Derived parameters from the small sample desert area. (a) Ratio σ_{HV}/σ_{HH}; (b) Dielectric constant; (c) Integrated surface roughness ks; (d) Elevation from AW3D30 DEM; (e) True-color image composite formed with bands 3 (red), 2 (green), 1 (blue); (f) False-color image composite formed with bands 7 (red), 4 (green), 1 (blue). (For interpretation of the references to color in this figure legend, the reader is referred to the web version of this article.)

elevation from the AW3D30 DEM, where the values in rock areas are much higher than those in the other areas. Fig. 7(e) is a true-color image composite formed with bands 3 (red), 2 (green), and 1 (blue). After a decorrelation-stretch (Gillespie, 1986), a false-color image composite formed with bands 7 (red), 4 (green), and 1 (blue) is generated in Fig. 7 (f). Finally, nine parameters, as depicted in Fig. 9, are selected for training the RF model.

Two RF parameters need to be determined when building the regression model, i.e., the number of stochastic variables in each decision tree (nsv) and the number of decision trees (ntree) (Breiman, 2001). The two parameters play important roles in determining the accuracy of the trained model. We first find the optimal value of nsv based on the traversal strategy where the traversal interval is set from 1 to 9 (i.e., the number of training parameters). Subsequently, the out-of-bag error (OOBE) (Breiman, 2001) is used to estimate the value of ntree. In the RF model, the nsv and ntree is set as 2 and 300, respectively.

About 10% of the total pixels are randomly selected from the sample area and used as the training sample to build the regression model. Subsequently, the remaining pixels in the area are used as the test sample to retrieve the penetration depth based on the model. Fig. 8(a) shows the scatter plot of the penetration depths derived from the IVM (Test value) and the predicted penetration depths (Predicted value). The correlation between the values is obvious, with the R^2 and the RMSE being 0.71 and 0.28 m, respectively. The pixels with SPDs ranging from

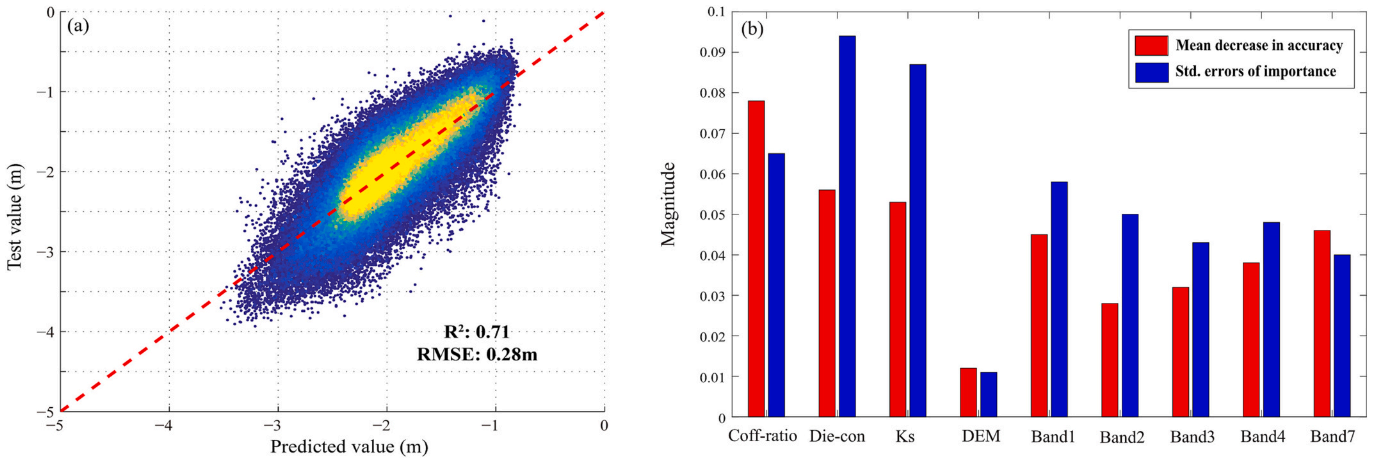

Fig. 8. (a) Scatter plot of the penetration depth derived from the coherence model (Test value) and the predicted penetration depth (Predicted value), the closer the color to yellow means that the greater the density of points; (b) The importance and its std. histogram of training parameters. (For interpretation of the references to color in this figure legend, the reader is referred to the web version of this article.)

−2.5 m to -1 m account for the majority of the test sample pixels. Fig. 8 (b) shows the mean decrease in accuracy for each variable, i.e., how the prediction accuracy of the RF model decreases when a variable is assigned a random value, indicating the importance of each variable. The more important a variable is, the larger the mean decrease in accuracy will be. The results indicate that the backscattering coefficient ratio is the most important in training the regression model, followed by the *ks* and ε. The reflectivities of bands 1, 4 and 7 are more important than the other three parameters, indicating that the mineral contents characterized by the composite images play useful roles. The standard deviation (std.) of each variable is simultaneously derived. To limit the difference between the ranges of the values, the std. is magnified 100 times when displayed. Among which the std. of *ks* and ε are higher than those of the other parameters. The std. of DEM is the smallest, only 10^{-3} (m).

4.3. Inversion of penetration depth for study area

The time intervals between the SAR images were nearly 30 days (see Table 2), the desert surface displacement should be taken into account in principle as the surface displacement could affect the SPD inversion. Surface displacement may have been caused by crustal deformation, groundwater exploitation and sand movement. However, there was no geological fault (URL: http://portal.onegeology.org/OnegeologyGlobal/) nor earthquake (URL: https://earthquake.usgs.gov/earthquakes/search/) reported between 29 July and 30 September 2008 in the study area. Deformation caused by groundwater withdrawal may only be at millimeter level per year (Hamling and Aoudia, 2011). The sand movement during the SAR acquisition is considered negligible for two reasons. First, the study site was relatively flat and was blocked by continuous ridges on three sides, therefore the sand medium was different from typical shifting dunes in deserts like Taklimakan Desert (Mamtimin et al., 2013). Second, the acquisition time of SAR images was the same as that for the sample InSAR pair. If there was significant surface displacement, serious decorrelation may have occurred in the sample area. We therefore assume that there was no ground deformation in the study area.

A supervised classification of the study area was performed before SPD inversion to analyze the SAR signal scattering mechanisms under different site conditions. The amplitudes of the HH- and HV- polarized images, the spectral information in optical images, the AW3D30 DEM and the SRTM C-band DEM were used in the Support Vector Machines (SVM) model for the classification. Four groups of features were classified as shown in Fig. 10(b). The overall accuracy of classification was 93.3% and the Kappa coefficient is 0.916. It was unnecessary to distinguish between the rock outcrops and the man-made features for the Jauf City area located in the NW corner of the study area as they had similar scattering responses in terms of the SAR signal penetrability.

The methods described in Section 3.3 were used to determine the scattering parameters and site features of the study area based on the SAR and optical images and the DEM. The backscattering coefficient ratio σ_{HV}/σ_{HH} in the sandy plains was much smaller than that for the rock outcrops (Fig. 9(a)) while the channels had the smallest values, indicating serious dissipation. As expected, the dielectric constant of the rocks was the highest among all the features, and that of the sandy plains was higher than that of the drainage channels because the complex mineral composite in the sandy plains may have increased the dielectric loss (Fig. 9(b) and (f)). The surface roughness parameter *ks*, which

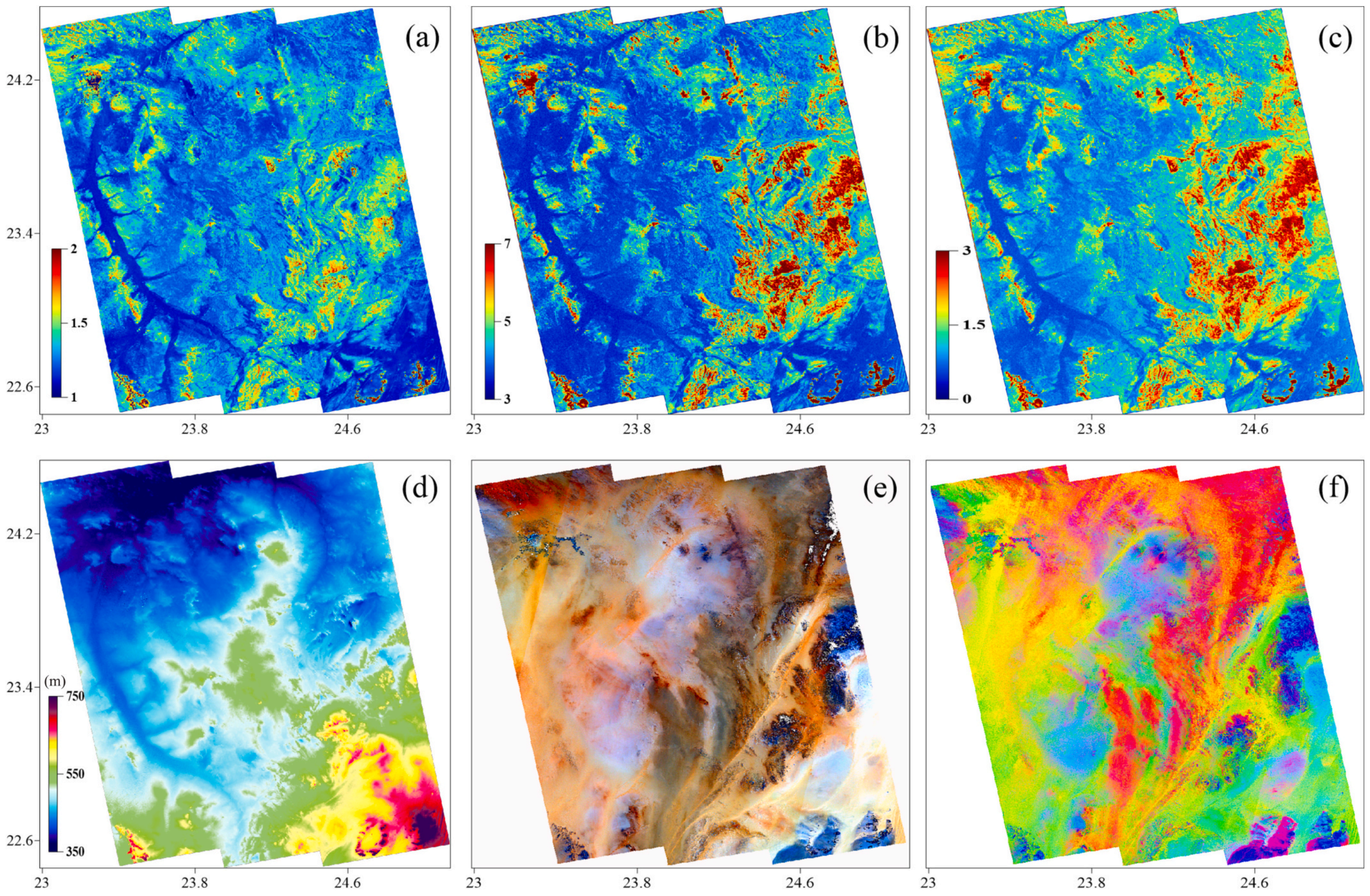

Fig. 9. Scattering parameters and site features of the study area. (a) Ratio of σ_{HV}/σ_{HH}; (b) Dielectric constant; (c) Surface roughness parameter; (d) Elevation from AW3D30 DEM; (e) True-color image composite formed with bands 3 (red), 2 (green) and 1 (blue); (f) False-color image composite formed with bands 7 (red), 4 (green) and 1 (blue). (For interpretation of the references to color in this figure legend, the reader is referred to the web version of this article.)

showed a similar trend as that of the dielectric constant, is shown in Fig. 9(c). The correspondence between the elevation and the types of the objects was obvious, especially over the paleochannels (Fig. 9(d)). Different types of objects were shown in the true-color image composite formed with bands 3 (red), 2 (green) and 1 (blue) (Fig. 9(e)). A decorrelation stretch (Gillespie, 1986) was deployed to the TM bands 7, 4 and 1 and a false color composite image for characterizing the mineral contents was generated by assigning red, green, and blue colors to the three bands, respectively (Fig. 9(f)).

The SPDs over the study area (Fig. 10(a)) were derived based on the trained RF model presented in Section 4.1. The SPD results varied between 1 m and 4 m over the study area, which were in good agreement with the features shown in the classification map. Several main channel systems in the left parts and the bottom-right corner could be observed. Details such as the small branches of the channels and the broken topography could also be clearly seen on the depth map. The average SPD in the rocks and the man-made features (visible on the composite true color optical image) slightly exceeded 1 m, which reflects the real penetration in, e.g., farmland and rocks partly covered by sand and may also be due to inherent errors caused by the applied IVM. The phenomenon will be further discussed in Sections 5.3 and 5.4. Penetration depths in the areas covered by sand sediments such as the sandy plains and channels varied significantly, ranging mainly from 1.5 m to 3.5 m that were attributed to the different physical properties of the areas. Three histograms of the SPDs are given in Fig. 11. We can find that the SPDs show a typical mean-centered normal distribution both in the channel and sandy plains, and the std. in different areas are almost the same.

4.4. Validation of the predicted penetration depth

In kufra basin, no penetration depth validation data sets like in situ measurements or other already published SPDs data can be obtained due to the harsh external environment. To verify the effectiveness and feasibility of the predicted penetration depth, we here added the scattering density maps to show the relationship and patterns between SPDs and training parameters (including backscattering coefficients ratio between HV and HH, dielectric constant, soil roughness, DEM and landcover), also the correlation coefficients were further calculated (Fig. 12).

Overall, a strong dependence between the predicted penetration depth and the external auxiliary parameters could be observed. The backscattering coefficients, dielectric constant and land surface roughness presented a stronger relevancy than the DEM, which was in line with the order of importance patterns shown in Fig. 8(b). Specifically, as shown in Fig. 12(a), with the ratio of σ_{HV}/σ_{HH} increased from 1 (channels and sandy plains) to 2 (rocks and man-made features), the SPDs decreased from 4 m to 0 m, which meant that the values of HV and HH backscattering coefficient were close in penetrable areas. The patterns between the dielectric constant and SPDs (Fig. 12(b)) are similar to that of soil roughness (Fig. 12(c)), as both parameters' value increase, the growth rate of the SPDs was fast to slow. Such two parameters were key information of radar capability to penetrate desert sand (Gaber et al., 2011). On the other hand, the value of the dielectric constant is concentrated between 3 and 6, and the value of the roughness is concentrated between 0.5 and 2, indicating that channels and sandy plains are the main features in the Kufra basin. The correlation coefficients between penetration depth and σ_{HV}/σ_{HH}, dielectric constant, soil roughness were 0.621, 0.636 and 0.630, respectively. In Fig. 12(d), a weaker correlation was displayed with a coefficient was 0.422. The SPDs reduced somewhat as the elevation increased from 400 m to 550 m. It was because a clear correspondence can be observed between elevation (Fig. 9(d)) and landcover in the channels and bedrocks (Fig. 10(b)), but was more ambiguous in sandy plains, which may be due to the distinctive topography of the Kufra Basin blocked by the three surrounding mountains. At last, the SPDs of different landforms had different concentrated distribution intervals (Fig. 12(e)), implying that the SPDs had a good response to the type of ground objects. The penetration in three landcover will be discussed in detail in Section 5.

5. Discussion

5.1. Penetration depth in channels

Geophysical exploration has found that there are some large paleochannels in the hyper-arid Kufra Basin, and some small buried paleochannels incised into the regional bedrocks (Mccauley et al., 1982). They could be formed in the Tertiary (Issawi, 1982) by the superposition

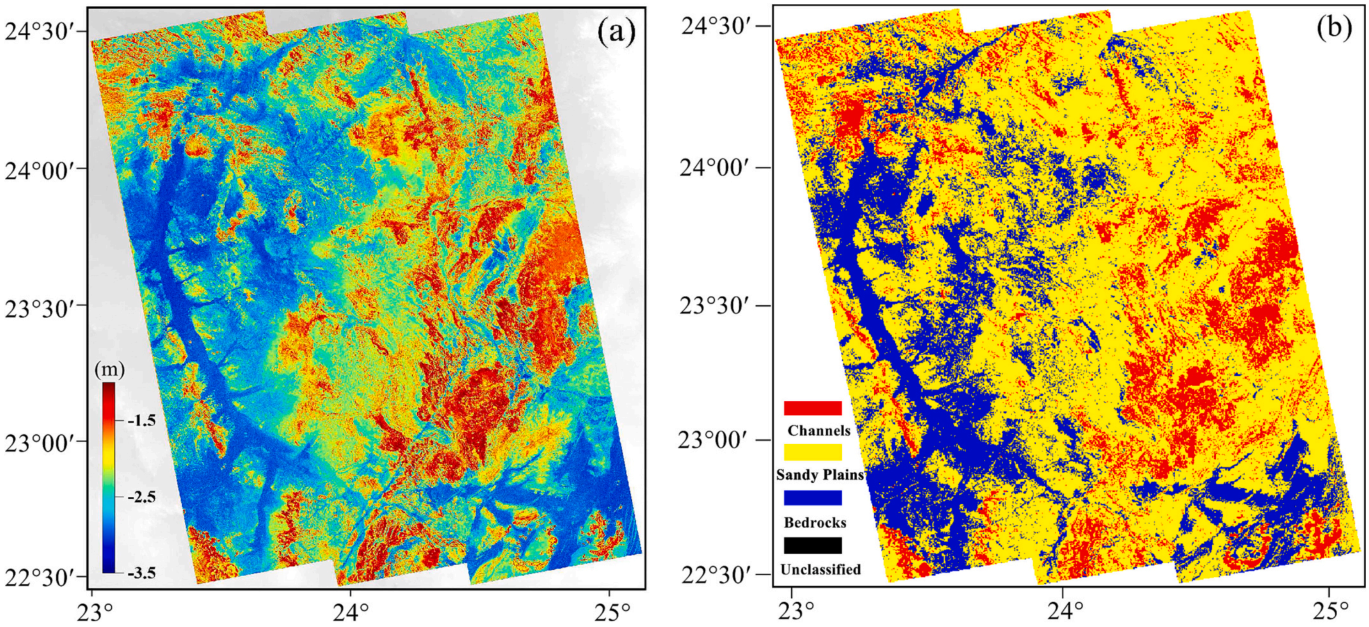

Fig. 10. (a) Penetration depth calculated from the proposed method; (b) Supervised classification of land cover into four categories, rocks and man-made features, sandy plains, channels and unclassified.

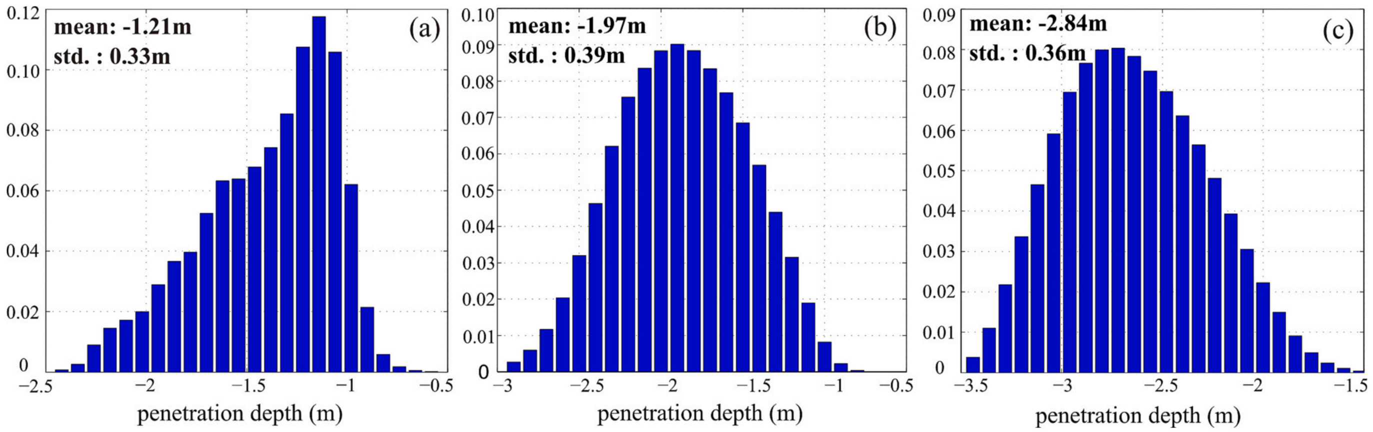

Fig. 11. Histograms of the calculated penetration depth. (a) Rocks and man-made features; (b) Sandy plains. (c) Channels.

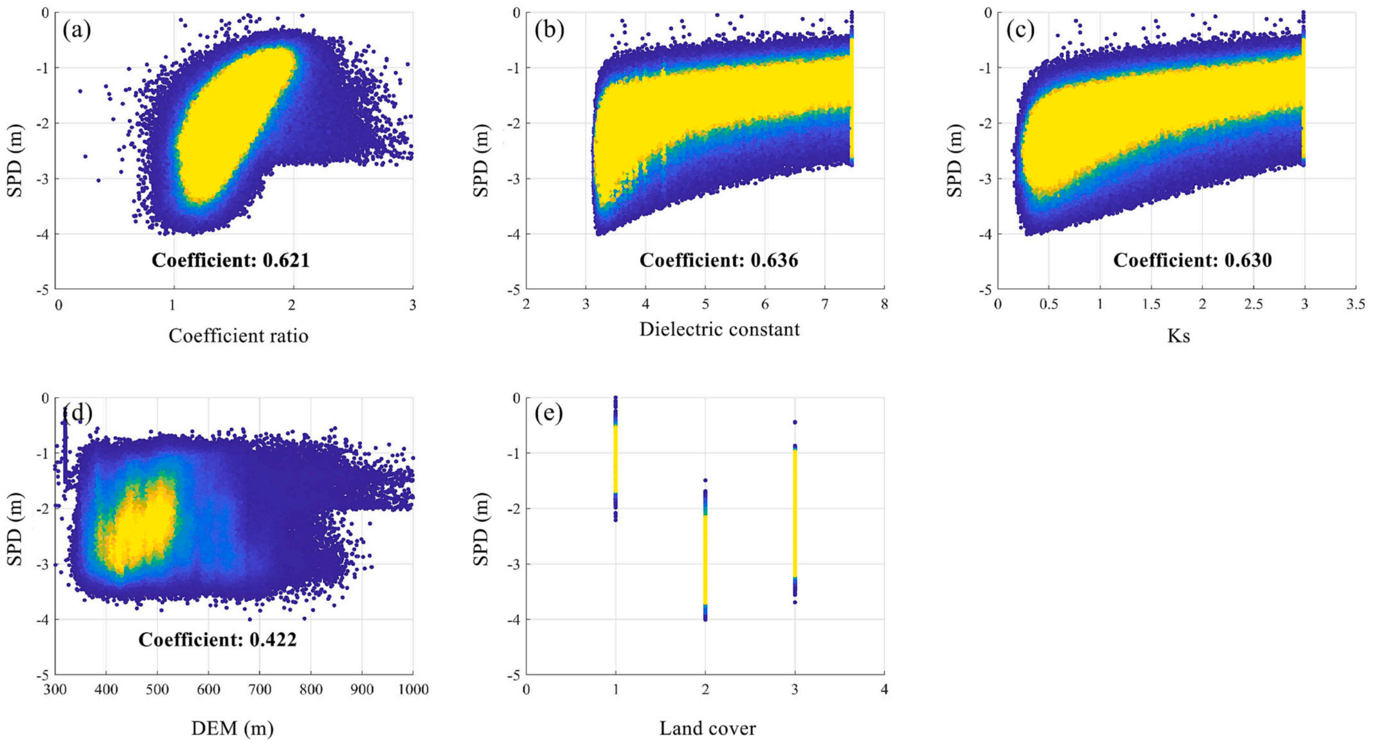

Fig. 12. Scatterplots between the predicted penetration depth and auxiliary parameters. (a) Ratio of σ_{HV}/σ_{HH}; (b) Dielectric constant; (c) Surface roughness parameter; (d) Elevation from AW3D30 DEM; (e) Land cover, the number 1 corresponds to bedrocks, 2 corresponds to channels and 3 corresponds to sandy plains.

of the fluvial and aeolian systems (Mainguet, 1992; El-Baz et al., 2000). The alluvial deposits may be formed in the last filling stage of the river-valley network and the riverbed became a low-lying depression in the late Quaternary (Mccauley et al., 1986a, 1986b) that appeared to be consistent with the elevation in the AW3D30 DEM. In the Landsat image (Fig. 9(e)), the filling of the paleochannels was mixed with the flat sandy plains and cannot be discriminated, as it had been fully covered by the wind-blown sand sheets. The river-valley filling was dark or mottled bright in the SAR amplitude images, which was in sharp contrast to the bright hues of the rock outcrops.

Almost all the surficial materials in the study area were from the Nubian strata, resulting in fine-grained aeolian and fluvial sediments. As shown in Fig. 9(e) and (f), the paleochannel areas were mostly covered by quartz particles (Xiong et al., 2017), showing a uniform or monotonous auratus hue that was quite different from the flat sandy plains. When the radar microwave penetrated through the surface sediments and encountered a rough subsurface, it imaged the subsurface and the imaging depth was the depth of the subsurface (Elachi and Granger, 2012). On the one hand, as the signal entered the paleochannels, its echo power attenuated significantly due to more scattering and absorption. Therefore, both the backscattering coefficients of HH- and HV-polarized images were smaller than those of the other landforms. The HH polarization performed better than the HV polarization in terms of echo power. On the other hand, since the filling of the paleochannels had more uniform particle sizes, the dielectric constant and roughness parameter were much smaller (Fig. 9(b) and (c)) than those of the sandy plains that consisted of complex materials (e.g., iron and manganese compounds and carbonate). The mean dielectric constant of the paleochannels was about 2.8, which was similar to that of the quartz-rich sand (Matzler and Murk, 2010). As a result, the signal penetrated more in the paleochannels as shown in Fig. 10(a). The SPDs in such areas mainly ranged from 2.5 m to 3.5 m, with an average of 2.84 m and an std. of

0.36 m, in excellent good agreement with results from other studies (Schaber et al., 1997; Schaber, 1999; Xiong et al., 2017) (Fig. 11(c)). Therefore, a sand layer of 2–3 m thick can be considered transparent to the L-band signal.

5.2. Penetration depth in sandy plains

Sandy plains dominated southwestern Egypt and northwestern Sudan (Breed et al., 1987), appearing monotonous in the Landsat images. Sandy plains covered the great majority of Kufra Basin with undulating sand ripples clearly seen in the true-color image (Fig. 9(e)). When assuming no significant surface displacement in the area, simple averaging could be made at the overlapping areas of the different paths of the SAR images. Different from the paleochannel areas, sandy plains appeared yellowish red to reddened hue on the false-color image (Fig. 9(f)) after decorrelation stretch, as the Nubia strata were ferruginized and varnished with manganese- and iron-oxide minerals (Davis et al., 1993). Spectral absorptions of Fe^{2+} (within 1.0–1.1 μm) , Fe^{3+} (strongest at 0.4 μm and weakest at 0.45 μm, 0.49 μm and 0.87 μm), CO_3^{2-} (within 2.0 μm and 2.5 μm) were used to discriminate the mineral content in the arid environment (Hunt and Salisbury, 1970, 1971; Hunt et al., 1971). The yellowish red to reddened hue colors were caused by Fe^{3+} (mostly hematite) that showed strong spectral absorption in band 1 and the redder areas indicated higher content of hematite (Fig. 9(f)). In addition, the dielectric dissipation of sand increased due to the increase of the hematite content (Matzler, 1998; Matzler and Murk, 2010), resulting in a higher dielectric constant compared with that of the paleochannels.

Peake and Oliver (1971) modified the Rayleigh criterion to define the different surface roughness. A surface was considered radar-smooth if $ks \leq 2\pi/25cos\theta$, radar-rough if $ks \geq 2\pi/4.4cos\theta$, and moderate radar-rough if ks falls between $2\pi/25cos\theta$ and$2\pi/4.4cos\theta$, where θ is the incidence angle. The ks of the sandy plains was mainly between 0.4 and 2.5, with the average ks being 1.62. Sandy plains were therefore defined as moderate radar-rough. In general, surface roughness has a positive effect on radar reflectivity. That is, the rougher a surface is, the stronger the radar reflectivity would be. This can explain why the reflectivity in the sandy plains are stronger than that in the channels. The backscattering coefficient of a sand layer was between that of the paleochannels and rock outcrops. When the radar signal penetrated the sandy plains, volume scattering dominated and the sand layer showed intermittent or mottled intermittent responses in the intensity images (Fig. 1(c)). Due to dielectric dissipation, the signal penetration was weaker than that in the paleochannel areas. Fig. 11(b) shows that the SPDs mainly ranged from 1.5 m to 2.5 m, with an average of 1.97 m and an std. of 0.39 m.

5.3. Penetration depth over the rock outcrops

Although most of the study area was covered by sand, there were also some rock outcrops whose elevations were higher than the surrounding areas, as shown in Fig. 9(d) and (e). The rock outcrops showed a distinct color in both the true- and false-color images, which were helpful for characterizing their mineral contents. For example, the bluish areas on the right and bottom left of the false-color image may contain a higher percentage of carbonate and sulfate (Fig. 9(f)) that showed strong adsorption of TM band 7 signal. The fuchsia color areas on the bottom right corner may have been caused by the strong absorption of band 4 signal by Fe^{2+} or its oxides.

The hard surfaces either on the surface or buried under the shallow sand may form single, dihedral or trihedral corner reflectors (Fung and Ulaby, 1983), leading to bright responses on the SAR amplitude images. The surfaces in these cases were extremely radar-rough. As shown in Fig. 9(c), almost all the ks in such areas ranged from 2 to 3.3 with an average of 2.62, larger than the threshold of $2\pi/4.4cos\theta$. The dielectric constant over the rock outcrops was obviously higher than the surrounding areas. Theoretically, no penetration should have occurred over the bare rock outcrops. However, the L-band SAR signal could easily penetrate the shallow sand that covered the rocks, leading to volume scattering and signal penetration. Inherent SPD biases may also exist since temporal decorrelation was not considered in the IVM used (Liu et al., 2020). Therefore, the derived SPDs over the rock outcrops were actually a result of both the thickness of the shallow sand and the possible model biases.

5.4. Penetration depth over man-made features

Most parts of the city were bare land although there were some residential areas, farms irrigated by the Nubian aquifer system (Robinson et al., 2006, 2007) and a grassland (Fig. 1(b) and Fig. 13(a)). The derived SPDs were depicted in Fig. 13(b). Both the buildings and rock outcrops could be regarded as hard surfaces for the L-band signal. The SPDs over the farmland and grassland were slightly larger than that over the buildings and rocks. We did not distinguish between the rocks and the man-made features as they had similar signal responses in terms of penetrability. The extracted scattering parameters such as the backscattering coefficient, dielectric constant and surface roughness were almost the same for the two types of features. The grassland and farmland were similar to the rocks covered by shallow sand. The small std. (about 0.33 m) also showed a small SPD difference between the features. The mean value −1.21 m shown in Fig. 11(a) was indeed the average of the SPD in both rocks and man-made features.

6. Conclusions

A new approach has been proposed for determining SAR signal penetration depth over large desert areas based on SPD from small sample areas and a ML model, which was helpful to complete a large-scale inversion when high-quality InSAR pairs were lacking in deserts.

The main findings of the study include,

(a) The approach appeared to have worked very well over the study area and it has overcome the difficulty of obtaining good-quality interferometric data over large desert areas for inverting SAR SPDs. The approach is useful for many applications of SAR over desert areas such as studying internal structures of sand.

(b) The proposed approach is based on a ML model and parameters including backscattering coefficient, dielectric constant, surface roughness, mineral content and land cover that can be reliably determined using optical and SAR remote sensing data jointly.

(c) Minerals such as hematite in the sand medium can increase the dielectric dissipation of the sand and shorten the penetration depth. Therefore, impact of mineral content in the sand should be considered when studying SPDs in a desert area.

New SAR satellite missions will offer greater capability for studying desert areas. For example, the upcoming ESA BIOMASS P-band SAR system will provide new opportunities for investigating deeper subsurface structures of deserts, like the buried Nubian aquifer system. The Tandem-L and LT-1 SAR will provide bistatic full-polarization data that will mean much reduced temporal decorrelation and atmospheric delays and better capability for analyzing the scattering mechanisms of SAR signals in the sand medium. Better retrieval of parameters such as the SPDs will be critically important for applications of the existing and new SAR missions in studying deserts.

CRediT authorship contribution statement

Jun Zhu: Conceptualization, Writing – original draft, Data curation. **Guanxin Liu:** Conceptualization, Writing – original draft, Methodology. **Rong Zhao:** Resources, Software, Writing – review & editing. **Xiaoli Ding:** Funding acquisition, Project administration, Writing – review & editing. **Haiqiang Fu:** Conceptualization, Writing – review & editing.

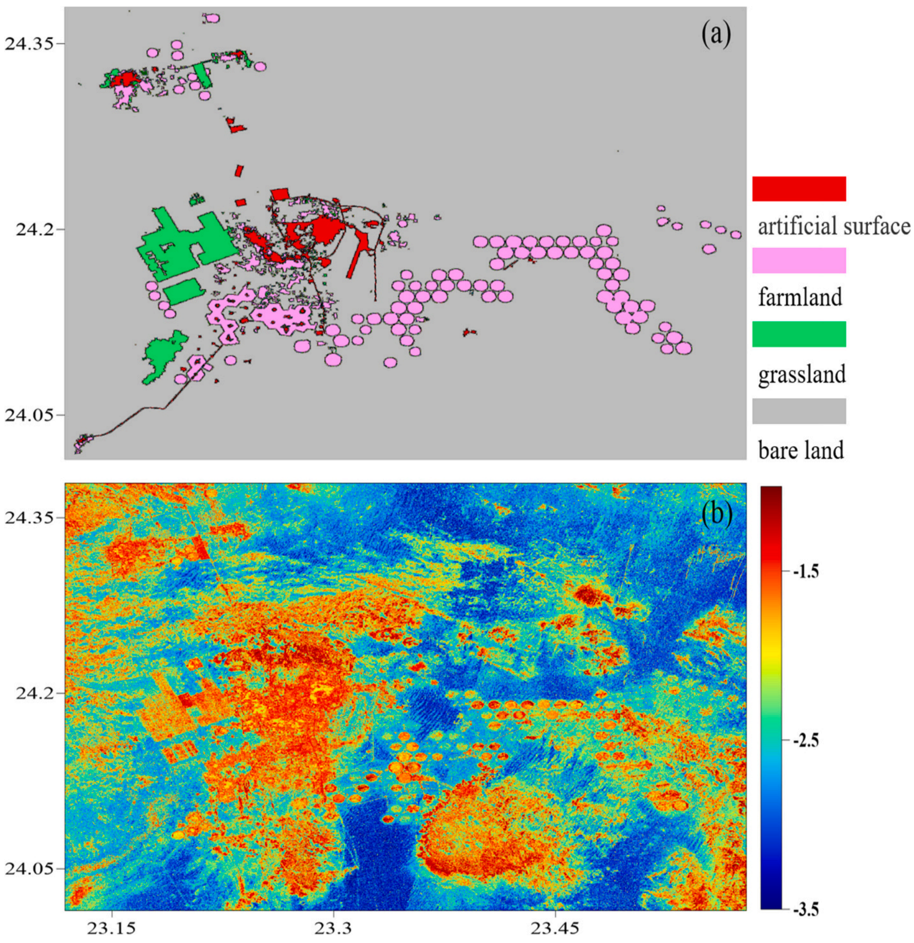

Fig. 13. (a) Land cover of Jauf city; (b) Penetration depth over the area.

Declaration of Competing Interest

The authors declare that they have no known competing financial interests or personal relationships that could have appeared to influence the work reported in this paper.

Data availability

The authors do not have permission to share data.

Acknowledgments

The authors would like to thank the Japanese Space Agency (JAXA) for providing the ALOS-1 data (URL: https://auig2.jaxa.jp/openam/UI/Login) and the AW3D30 DEM data (URL: https://www.eorc.jaxa.jp/ALOS/en/aw3d30/data/index.htm), and the National Aeronautics and Space Administration (NASA) for providing the Landsat 5 TM data (URL: https://earthexplorer.usgs.gov). The research was supported by the Research Grants Council (RGC) of the Hong Kong Special Administrative Region (PolyU 152164/18E and PolyU 152233/19E), the Research Institute for Sustainable Urban Development (RISUD), The Hong Kong Polytechnic University, and the Innovative Technology Fund (ITP/019/20LP).

Appendix A. Supplementary data

Supplementary data to this article can be found online at https://doi.org/10.1016/j.rse.2023.113643.

References

Ali, E.S., Xu, W.B., Ding, X.L., 2020. Improved optical image matching time series inversion approach for monitoring dune migration in North Sinai Sand Sea: algorithm procedure, application, and validation. ISPRS J. Photogramm. Remote Sens. 164 (1), 106–124. https://doi.org/10.1016/j.isprsjprs.2020.04.004.

Ali, E.S., Xu, W.B., Ding, X.L., 2021. Spatiotemporal variability of dune velocities and corresponding uncertainties, detected from optical image matching in the North Sinai Sand Sea, Egypt. Remote Sens. 13 (18) https://doi.org/10.3390/rs13183694.

Ali, E.S., Xu, W.B., Xie, L., Ding, X.L., 2022. Assessment of aeolian activity in the Bodélé Depression, Chad: a dense spatiotemporal time series from Landsat-8 and Sentinel-2 Data. Front. Environ. Sci. https://doi.org/10.3389/fenvs.2021.808802.

Archer, D.J., Wadge, G., 2001. Modeling the backscatter response due to salt crust development. IEEE Trans. Geosci. Remote Sens. 39, 2307–2310.

Banda, F., Dall, J., Tebaldini, S., 2016. Single and multipolarimetric P-band SAR tomography of subsurface ice structure. IEEE Trans. Geosci. Remote Sens. 54 (5), 2832–2845.

Breiman, 2001. Random forests. Mach Learn. 45 (1), 5–32.

Breed, C.S., McCauley, J.F., Davis, P.A., 1987. Sand sheets of the eastern Sahara and ripple blankets on Mars. Geol. Soc. Lond. Spec. Publ. 35, 337–359.

Charlton, M.B., White, K., 2006. Sensitivity of radar backscatter to desert surface roughness. Int. J. Remote Sens. 27, 1641–1659.

Dall, J., 2007. InSAR elevation bias caused by penetration into uniform volumes. IEEE Trans. Geosci. Remote Sens. 45, 2319–2324.

Dan, G.B., 1998. Remote sensing of desert dune forms by polarimetric synthetic aperture radar (SAR). Remote Sens. Environ. 65, 204–216.

Davis, P.A., Breed, C.S., McCauley, J.F., Schaber, G.G., 1993. Surficial geology of the safsaf region, south-Central Egypt, derived from remote-sensing and field data. Remote Sens. Environ. 46, 183–203.

Dobson, M.C., Ulaby, F.T., Hallikainen, M.T., El-rayes, M.A., 1985. Microwave dielectric behavior of wet soil-part II: dielectric mixing models. IEEE Trans. Geosci. Remote Sens. GE-23, 35–46.

Elsherbini, A., Sarabandi, K., 2010. Mapping of sand layer thickness in deserts using SAR interferometry. IEEE Trans. Geosci. Remote Sens. 48, 3550–3559.

Elachi, Charles, Roth, Ladislav, E., Schaber, Gerald, G., 1984. Spaceborne Radar Subsurface Imaging in Hyperarid Regions. Geosci. Remote Sens. IEEE Trans. On GE-22, 383–388.

El-Baz, F., Maingue, M., Robinson, C., 2000. Fluvio-aeolian dynamics in the North-Eastern Sahara: the relationship between fluvial/aeolian systems and ground-water concentration. J. Arid Environ. 44, 173–183.

Elachi, C., Granger, J., 2012. Spaceborne imaging radars probe 'in depth'. IEEE Spectr. 19, 24–29.

Farr, T.G., Elachi, C., Hartl, P., Chowdhury, K., 1986. Microwave penetration and attenuation in desert soil: a field experiment with the shuttle imaging radar. IEEE Trans. Geosci. Remote Sens. GE-24, 590–594.

Fung, A.K., Ulaby, F.T., 1983. Matter-energy interaction in the microwave region. In: Manual of Remote Sensing. Amer. Soc. Photogrammetry, VA, Falls Church, pp. 115–144.

Guo, H.D., Schaber, G.G., Breed, C.S., 1986. Shuttle imaging radar response from. sand and subsurface rocks of Alashan Plateau in north-central China. In: Int. Symp. on Remote Sensing for Resources Development and Environmental Management, pp. 137–143.

Guo, H., Liu, H., Wang, X., Shao, Y., Yan, S., 2000. Subsurface old drainage detection and paleoenvironment analysis using spaceborne radar images in alxa plateau. Sci. China Ser. Earth Sci. 43, 439–448.

Ghoneim, E., El-Baz, F., 2007. The application of radar topographic data to mapping of a mega-paleodrainage in the eastern Sahara. J. Arid Environ. 69, 658–675.

Gaber, A., Amarah, B.A., Abdelfattah, M., Ali, S., 2017. Investigating the use of the dual-polarized and large incident angle of SAR data for mapping the fluvial and aeolian deposits. Nriag J. Astron. Geophys. 9, 349–360.

Gaber, A., Koch, M., Griesh, M.H., Sato, M., 2011. SAR remote sensing of buried faults: implications for groundwater exploration in the Western Desert of Egypt. Sens. Imaging Int. J. 12, 133–151.

Gillespie, A.R., 1986. Color enhancement of highly correlated images. I. Decorrelation and HSI contrast stretches. Remote Sens. Environ. 20, 209–235.

Hallikainen, M.T., Ulaby, F.T., Dobson, M.C., El-rayes, M.A., Wu, L., 1985. Microwave dielectric behavior of wet soil-part 1: empirical models and experimental observations. IEEE Trans. Geosci. Remote Sens. GE-23, 25–34.

Hamling, I.J., Aoudia, A., 2011. Interaction between the North-West Sahara Aquifer and the seismically active intraplate Hun Graben Fault system, Libya. In: Proceedings of the American Geophysical Union (AGU) Fall Meeting, San Francisco, CA, USA, pp. 5–9.

Hoekstra, P., Delaney, A., 1974. Dielectric properties of soils at UHF and microwave frequencies. J. Geophys. Res. 79, 1699–1708.

Hermina, M., 1990. The surroundings of kharga, Dakhla and farafra oases. In: The Geology of Egypt. Taylor & Francis Group, CRC Press, Boca Raton, FL, USA, pp. 259–292.

Hunt, G.R., Salisbury, J.W., 1971. Visible and near infrared spectra of minerals and rocks. II. Carbonates. Mod. Geol. 2, 23–30.

Hunt, G.R., Salisbury, J.W., 1970. Visible and near-infrared spectra of minerals and rocks: I silicate minerals. Mod. Geol. 1, 283–300.

Hunt, G.R., Salisbury, J.W., Lenhoff, C.J., 1971. Visible and near infrared spectra of minerals and rocks: III. Oxides and hydroxides. Mod. Geol. 2, 195–205.

Issawi, B., 1982. Geology of the southwestern desert of Egypt.

Liu, G., Fu, H., Zhu, J., Wang, C., Xie, Q., 2020. Penetration depth inversion in Hyperarid Desert from L-band InSAR data based on a coherence scattering model. IEEE Geosci. Remote Sens. Lett. 99, 1–5.

Lüning, S., Craig, J., Fitches, B., Mayouf, J., Mcilroy, D., 1999. Re-evaluation of the petroleum potential of the Kufra Basin (SE Libya, ne Chad): does the source rock barrier fall? Mar. Pet. Geol. 16, 693–718.

Mamtimin, A., Miao, Q.L., Jin, L.L., et al., 2013. Characteristics of diffuse radiation at hinterland of the taklimakan desert. J. Desert Res. 33 (5), 1492–1500.

Matzler, C., 1998. Microwave permittivity of dry sand. IEEE Trans. Geosci. Remote Sens. 36, 319.

Matzler, C., Murk, A., 2010. Complex dielectric constant of dry sand in the 0.1 to 2 GHz range. Tech Rep.

Mccauley, J.F., Schaber, G.G., Breed, C.S., Grolier, M.J., Haynes, C.V., Issawi, B., Elachi, C., Blom, R., 1982. Subsurface valleys and geoarcheology of the eastern Sahara revealed by shuttle radar. Science 218, 1004–1020.

Mainguet, M., 1992. A global open wind action system: the Sahara and the Sahel. Int. Conf. Geol. Arab World 33–42.

Mccauley, J.F., Breed, C.S., Schaber, G.C., 1986. The megageomorphology of the radar Rivers of the eastern Sahara. Second Spaceborne Imaging Radar Symp. 25–35.

Mccauley, J.F., Breed, C.S., Schaber, G.G., Mchugh, W.P., Issawi, B., Haynes, C.V., Grolier, M.J., Kilani, A.E., 1986. Paleodrainages of the eastern Sahara-the radar Rivers revisited (SIR-A/B implications for a mid-tertiary trans-afnrcan drainage System). IEEE Trans. Geosci. Remote Sens. GE-24, 624–648.

Natale, A., Esposito, C., Berardino, P., Lanari, R., Perna, S., 2019. Retrieval of Soil Surface Parameters via Helicopter-Borne P-Band Polarimetric SAR Data Acquired Along Antiparallel Flight Tracks. In: IGARSS 2019 - 2019 IEEE International Geoscience and Remote Sensing Symposium, pp. 7002–7005.

Oh, Y., 2004. Quantitative retrieval of soil moisture content and surface roughness from multipolarized radar observations of bare soil surfaces. Geosci. Remote Sens. IEEE Trans. 42, 596–601.

Paillou, P., Schuster, M., Tooth, S., Farr, T., Rosenqvist, A., Lopez, S., Malezieux, J.M., 2009. Mapping of a major paleodrainage system in eastern Libya using orbital imaging radar: the Kufrah River. Earth Planet. Sci. Lett. 277, 327–333.

Paillou, P., Grandjean, G., Baghdadi, N., Heggy, E., Achache, J., 2003. Subsurface imaging in south-Central Egypt using low-frequency radar: bir safsaf revisited. IEEE Trans. Geosci. Remote Sens. 41, 1672–1684.

Peake, W.H., Oliver, T.L., 1971. The response of terrestrial surfaces at microwave frequencies. Response Terr. Surf. Microw. Freq. 1440–1447.

Robinson, C.A., El-Baz, F., Al-Saud, T., Jeon, S.B., 2006. Use of radar data to delineate palaeodrainage leading to the Kufra oasis in the eastern Sahara. J. Afr. Earth Sci. 44, 229–240.

Robinson, C.A., Werwer, A., El-Baz, F., El-Shazly, M., Fritch, T., Kusky, T., 2007. The Nubian aquifer in Southwest Egypt. Hydrogeol. J. 15, 33–45.

Schlund, M., Baron, D., Magdon, P., Erasmi, S., 2019. Canopy penetration depth estimation with TanDEM-X and its compensation in temperate forests. ISPRS J. Photogramm. Remote Sens. 147, 232–241.

Schaber, G.G., Mccauley, J.F., Breed, C.S., 1997. The use of multifrequency and polarimetric SIR-C/X-SAR data in geologic studies of Bir Safsaf, Egypt. Remote Sens. Environ. 59, 337–363.

Schaber, G.G., Mccauley, J.F., Breed, C.S., Olhoeft, G.R., 1986. Shuttle imaging radar: physical controls on signal penetration and subsurface scattenng in the eastern Sahara. IEEE Trans. Geosci. Remote Sens. GE-24, 603–623.

Schaber, G.G., 1999. SAR studies in the Yuma Desert, Arizona - physical controls on signal penetration and subsurface scattering in the eastern Sahara. Remote Sens. Environ. 67, 320–347.

Sharma, J.J., Hajnsek, I., Papathanassiou, K.P., Moreira, A., 2013. Estimation of glacier ice extinction using long-wavelength airborne pol-InSAR. IEEE Trans. Geosci. Remote Sens. 51 (6), 3715–3732.

Sternberg, T., Paillou, P., 2015. Mapping potential shallow groundwater in the Gobi Desert using remote sensing: Lake ulaan nuur. J. Arid Environ. 118, 21–27.

Satgé, F., Bonnet, M.P., Timouk, F., et al., 2015. Accuracy assessment of SRTM v4 and ASTER GDEM v2 over the altiplano watershed using ICESat/GLAS data[J]. Int. J. Remote Sens. 36 (2), 465–488.

Topp, G.C., Davis, J.L., Annan, A.P., 1980. Electromagnetic determination of soil water content: measurements in coaxial transmission lines. Water Resour. Res. 16, 574–582.

Ulaby, F.T., Moore, R.K., Fung, A.K., 1981. Microwave remote sensing: Active and passive. Volume 1 - Microwave remote sensing fundamentals and radiometry [M]. Artech House 1–456.

United States Geological Survey (USGS), 2022. What is a desert? https://pubs.usgs.gov/gip/deserts/what/ retrieved 6 November 2022.

Wang, R., Cheng, H., Tao, Z., Teng, L., Ke, Y., 2014. Subsurface height measurement using InSAR technique in sand-covered arid areas. Geosci. Remote Sens. Symp. 422–424.

Wang, R., Muller, J.P., Hu, C., Zeng, T., 2015. Comparison between SRTM-C DEM and ICESAT elevation data in the arid Kufrah area. IET Int. Radar Conf. 1–4.

Xiong, S., Jan-Peter, M., Gang, L., 2017. The application of ALOS/PALSAR InSAR to measure subsurface penetration depths in deserts. Remote Sens. 9, 638.

Yu, C., Li, Z., Penna, N.T., Crippa, P., 2018. Generic atmospheric correction model for interferometric synthetic aperture radar observations. J. Geophys. Res. Solid Earth 123 (10), 9202–9222.